Supporting Information

Efficient Doped and Non-doped Light-Emitting Diodes Based on a TADF-Emitting Cu_4Br_4 Cluster

Xin Lu,[abc] Shao-Jie Wu,[abc] Ya-Shu Wang,[bc] Shan-Yue Wei,[cd] Lingyi Meng,[abc] Xi-He Huang,*[a] Xu-Lin Chen,*[abc] and Can-Zhong Lu*[abc]

[a] College of Chemistry, Fuzhou University, Fuzhou, Fujian 350108, China

[b] State Key Laboratory of Structural Chemistry, Fujian Institute of Research on the Structure of Matter, Chinese Academy of Sciences, Fuzhou, Fujian 350002, China

[c] Xiamen Key Laboratory of Rare Earth Photoelectric Functional Materials, Xiamen Institute of Rare-earth Materials, Haixi Institutes, Chinese Academy of Sciences, Xiamen, Fujian 361021, China

[d] Engineering Research Center of Environment-Friendly Function Materials, Ministry of Education, Institute of Materials Physical Chemistry, Huaqiao University, Xiamen 361021, P. R. China.

E-mail: xlchem@fjirsm.ac.cn; xhhuang@fzu.edu.cn; czlu@fjirsm.ac.cn

Table of Contents

1 General Methods S3

2 Material Synthesis and Characterization S4

3 X-ray structure determination S5

4 Computational methodology and results S7

5 Thermogravimetric Analysis (TGA) S9

6 Cyclic Voltammetry S10

7 Photophysical Properties S11

8 Device Fabrication and Characterization S14

9 NMR Spectra S16

10 Reference S19

1 General Methods

All air and moisture sensitive reactions are carried out in an argon atmosphere. Unless otherwise specified, all starting materials used are commercially available and require no further purification. The reaction solvents used in the reaction are all commercial analytical pure reagents, and some of the reagents have been dried by molecular sieve (4 Å) before use. The prepared TADF material is twice dried and recrystallized before the device is manufactured. ^{1}H NMR and ^{13}C NMR were obtained using a Bruker Avance III nuclear magnetic resonance spectrometer at a frequency of 500 Hz in deuterated chloroform ($CDCl_3$) and deuterated dimethyl sulfone (DMSO) solution. Thermogravimetric analysis (TGA) was performed by TGA/DSC in a nitrogen atmosphere at a heating rate of 10 K/min. Single crystal X-ray diffraction data were collected on a Bruker-D8 VENTRUE diffractometer with an X-ray source of Mo $k\alpha$. Cyclic voltammetry (CV) was performed by CHI840D electrochemical analyzer. The UV-VIS absorption spectra were recorded by Agilent Cary 5000 UV-VIS spectrophotometer under ambient conditions. Fluorescence quantum yields were measured using FluoroMax-4 fluorescence spectrometers equipped with integrating spheres. Xenon lamp was used as a light source to record the steady-state PL spectra on Edinburgh FLS980. Using NT242-1K OPO laser as excitation source, the transient PL attenuation curves of samples were recorded in time-dependent single photon counting mode at Edinburgh FLS980.

2 Material Synthesis and Characterization

Scheme S1 Synthetic route of AcNP and $Cu_4Br_4(AcNP)_2$.

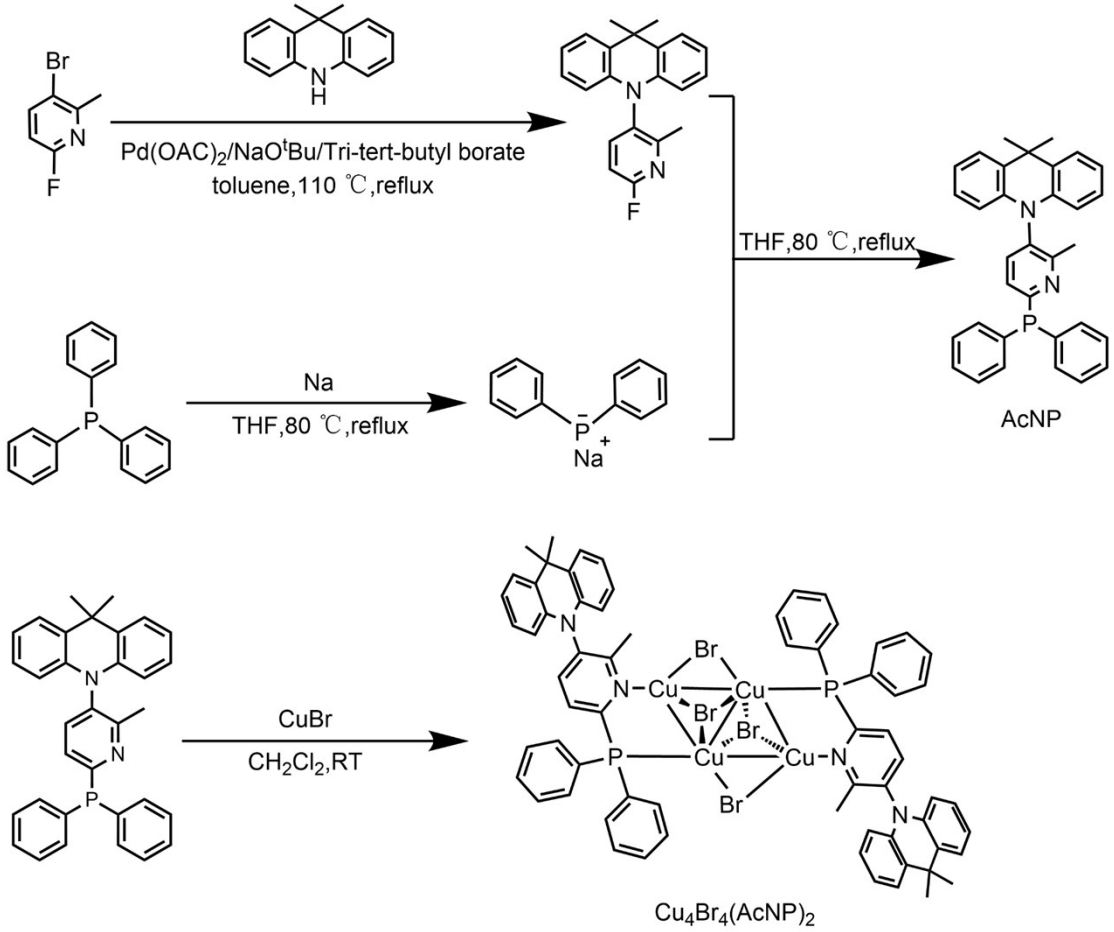

10-(6-fluoro-2-methylpyridin-3-yl)-9,9-dimethyl-9,10-dihydroacridine: The synthesis process was referred to the reported literature. [1]

sodium diphenylphosphide: The synthesis process was referred to the reported literature.[2]

AcNP: 10-(6-fluoro-2-methylpyridin-3-yl)-9,9-dimethyl-9,10-dihydroacridine (3.18 g, 10 mmol) was placed in 100 ml dry double-necked Schlenk tube in an argon atmosphere. The tetrahydrofuran solution of sodium diphenylphosphide (20 ml, 30 mmol) prepared by the above reaction is then slowly injected into the Schlenk tube, Stir at 80 ℃ overnight. The reaction mixture is quenched with methanol and the solvent is evaporated under reduced pressure. The product was purified by column chromatography on silica gel using petroleum ether/ dichloromethane (10:1) as the eluent to afford a white solid (3.65 g, yield: 75%). ^{1}H NMR (500 MHz, Chloroform-d) δ 7.59 – 7.37 (m, 13H), 7.11 (d, J = 7.9 Hz, 1H),

7.05 – 6.93 (m, 4H), 6.10 (dd, J = 8.1, 1.4 Hz, 2H), 2.37 (s, 3H), 1.71 (d, J = 40.5 Hz, 6H).

$Cu_4Br_4(AcNP)_2$: At room temperature, the mixture of AcNP (484mg, 1mmol) and CuBr (287mg, 2mmol) was stirred in 5ml CH_2Cl_2 solution for 2 hours. The clarified solution was obtained by filtration, and the yellow cuprous complex single crystal was obtained by slow diffusion of ether in CH_2Cl_2 solution, which was suitable for X-ray diffraction measurement, yield: 55%. ^{1}H NMR (500 MHz, DMSO-d_6) δ 7.94 – 7.86 (m, 2H), 7.68 (t, J = 8.8 Hz, 8H), 7.51 (dt, J = 15.5, 7.6 Hz, 18H), 6.96 (dt, J = 25.3, 7.4 Hz, 8H), 5.95 (d, J = 8.0 Hz, 4H), 2.18 (d, J = 2.8 Hz, 6H), 1.67 (s, 6H), 1.57 (s, 6H). ^{13}C NMR (126 MHz, DMSO) δ 159.37, 159.27, 157.34, 156.98, 140.14, 138.26, 138.19, 134.92, 134.19, 134.08, 132.13, 132.02, 131.89, 131.57, 131.50, 130.25, 129.52, 129.46, 129.23, 129.04, 128.60, 128.54, 126.91, 126.81, 126.09, 121.06, 120.96, 112.54, 112.48, 40.57, 40.40, 40.24, 40.07, 39.90, 39.73, 39.57, 35.36, 32.97, 31.35, 20.24.

3 X-ray structure determination

Table S1 Crystal parameters and refinement data of $Cu_4Br_4(AcNP)_2$

Complex	$Cu_4Br_4(AcNP)_2$
Empirical formula	$C_{66}H_{58}Br_4Cu_4N_4P_2$
Formula weight	1542.90
Temperature/K	200.0
Crystal system	monoclinic
Space group	$P2_{1/c}$
a/Å	12.4898(6)
b/Å	14.4877(6)
c/Å	16.7458(7)
α/°	90
β/°	96.065(2)
γ/°	90
Volume/Å^3	3013.2(2)
Z	4

ρ_{calcg}/cm^3	1.701
μ/mm^{-1}	4.143
F (000)	1536.0
Crystal size/mm^3	0.2 × 0.2 × 0.2
Radiation	Mo K_α (λ = 0.71073)
2Θ range for data collection/°	5.132 to 55.12
Index ranges	-16 ≤ h ≤ 16, -18 ≤ k ≤ 18, -21 ≤ l ≤ 21
Reflections collected	60621
Independent reflections	6950 [R_{int} = 0.1418, R_{sigma} = 0.0729]
Data/restraints/parameters	6950/0/364
Goodness-of-fit on F^2	1.028
Final R indexes [I>=2σ (I)]	R_1 = 0.0649, wR_2 = 0.1536
Final R indexes [all data]	R_1 = 0.1185, wR_2 = 0.1872
Largest diff. peak/hole / e $Å^{-3}$	3.12/-0.94

Table S2 Selected bond length (Å) and bond angles (deg) of $Cu_4Br_4(AcNP)_2$

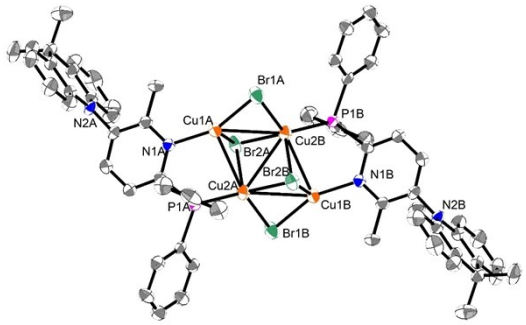

Br1A-Cu1A	2.2914(12)
Br1A-Cu2A	2.4890(12)
Br2A-Cu1B	2.6124(14)
Br2A-Cu2A	2.6236(13)
Br2A-Cu2A	2.5543(12)
Cu1A-Br1B	2.2915(12)
Cu1A-Br2B	2.6123(14)
Cu1A-Cu2A	2.8128(14)

Cu1A-Cu2B	2.9063(13)
Cu1A-N1A	1.951(6)
Cu2A-Br2B	2.6237(13)
Cu2A-Cu1B	2.9064(13)
Cu2A-Cu2B	2.8898(18)
Cu2A-P1A	2.2371(19)
Cu1B-Br1A-Cu2A	74.76(4)
Cu2A-Cu1A-Cu2B	60.67(4)
N1A-C-P1A	112.5(5)

4 Computational methodology and results

The density functional theory (DFT) and time-dependent DFT (TD-DFT) calculations were performed with the Gaussian 09 program package.[3] The density functional theory (DFT) calculations at the B3LYP/6-31G* level was used to optimize the ground state geometries of the investigated compounds. Time-dependent density functional theory (TD-DFT) calculations was performed at the same level using the optimized ground state geometries. The electron density diagrams of molecular orbitals were generated using GaussView program. The partition orbital composition was analyzed with the Multiwfn 2.4 program.[4]

Table S3 Composition of the frontier orbitals of $Cu_4Br_4(AcNP)_2$.

	Cu	Br	ligand
HOMO	65.14%	21.35%	13.52%
LUMO	5.07%	0.99%	95.94%

Table S4 Natural transition orbit (NTOs) and orbital contribution of $Cu_4Br_4(AcNP)_2$ in excited states.

state	main contribution	natural transition orbital
S_1	HOMO→LUMO (44.26%), HOMO→LUMO+1(25.05%), HOMO-1→LUMO (17.93%)	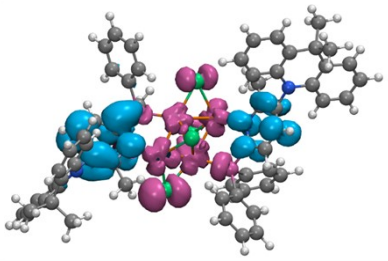
T_1	HOMO→LUMO+1(82.77%)	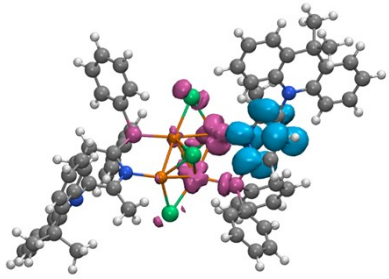
T_2	HOMO→LUMO (37.20%), HOMO-1→LUMO (34.30%), HOMO-3→LUMO (13.53%)	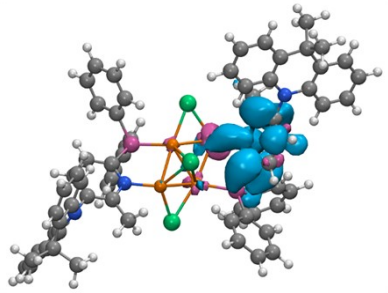
T_3	HOMO-1→LUMO (44.92%), HOMO→LUMO (17.19%), HOMO-6→LUMO (11.81%)	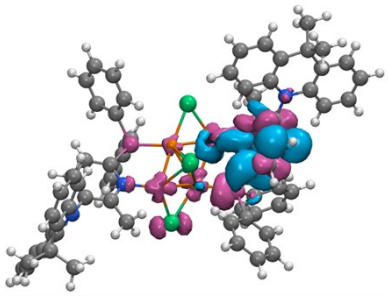
T_4	HOMO-3→LUMO (31.92%), HOMO→LUMO (30.62%), HOMO-2→LUOM (25.70%)	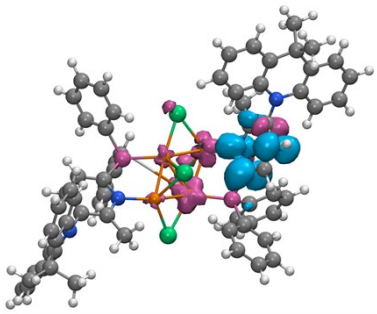

Table S5 Compositions of hole and electron in the S_1 and T_1 of $Cu_4Br_4(AcNP)_2$.

		Cu	Br	ligand
S_1	hole	64.58%	10.96%	24.46%
	electron	9.64%	1.61%	88.75%
	difference	54.94%	9.35%	-64.23%
T_1	hole	64.57%	17.20%	18.23%
	electron	19.94%	10.00%	70.06%
	difference	44.63%	7.20%	-51.83%

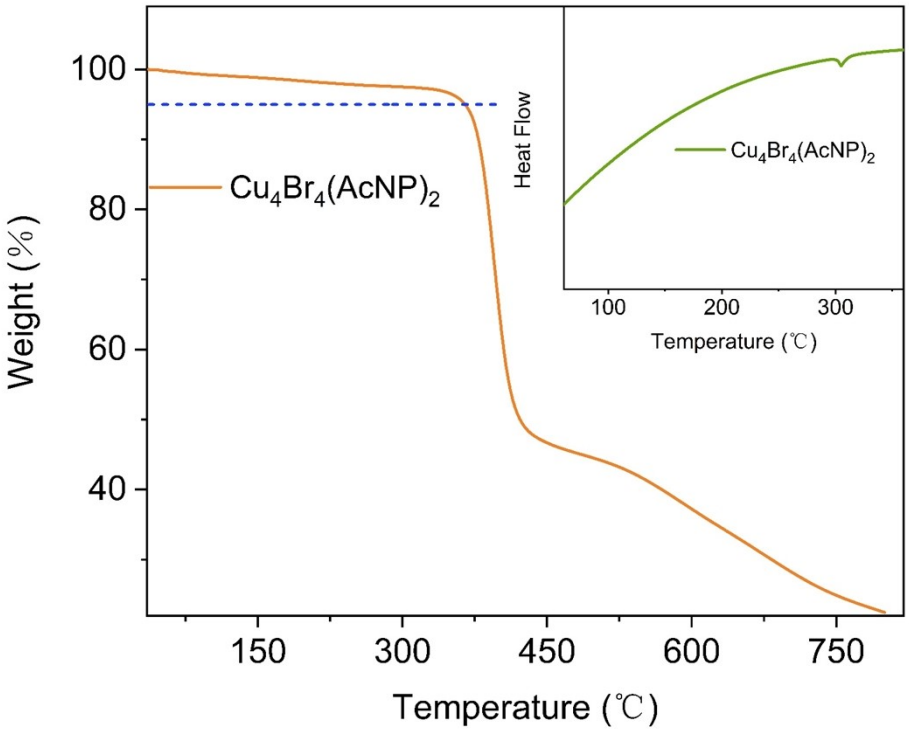

5 Thermogravimetric Analysis (TGA)

Fig. S1 TGA curve and Tg curve of A. The dashed blue line represents 95% of the weight of the original sample.

6 Cyclic Voltammetry

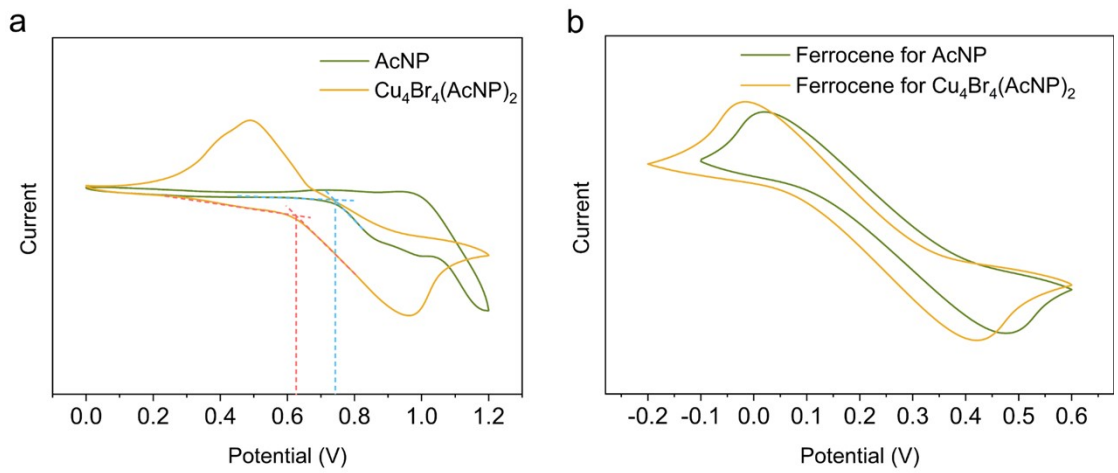

Fig. S2 a) Cyclic voltammetry curves of AcNP and $Cu_4Br_4(AcNP)_2$ in dichloromethane at room temperature; b) Cyclic voltammetry curves of ferrocene (internal standard).

Cyclic voltammetry was performed at room temperature in anhydrous and argon-saturated dichloromethane solutions of 0.1 M tetrabutylammonium hexafluorophosphate and 1.0 mM investigated compounds with a CHI840D electrochemical analyzer. Glassy carbon, platinum wire and Ag/Ag^+ (0.01 M of $AgNO_3$ in acetonitrile) were selected as the working electrode, auxiliary electrode and reference electrode, respectively. The ferrocenium/ferrocene couple was used as an internal standard. The HOMO and LUMO energy levels were estimated from the cyclic voltammetry and optical bandgaps (E_g) determined from the onset of the absorption band (λ_{onset}).

Table S6 Summary of CV data and energy levels.

Compound	E_{OX} [a] [eV]	$E_{Fc/Fc+}$ [b] [eV]	E_g [c] [eV]	E_{HOMO} [d] [eV]	E_{LUMO} [e] [eV]
AcNP	0.74	0.26	3.17	-5.28	-2.11
$Cu_4Br_4(AcNP)_2$	0.63	0.21	2.86	-5.22	-2.36

[a] the oxidation potentials (E_{OX}) were acquired from the onset of first oxidation potentials in cyclic voltammograms (see Fig. S2); [b] ferrocenium/ferrocene couple was used as an internal standard; [c] calculated from the absorption edge λ_{onset} (see Fig. S3) using equation:

1241/λ_{onset}; [d] calculated using the equation: E_{HOMO} = - [E_{OX}- $E_{Fc/Fc+}$ + 4.8] eV; [e] calculated from E_g and E_{HOMO} using the equation: E_{LUMO} = (E_{HOMO} + E_g) (eV).

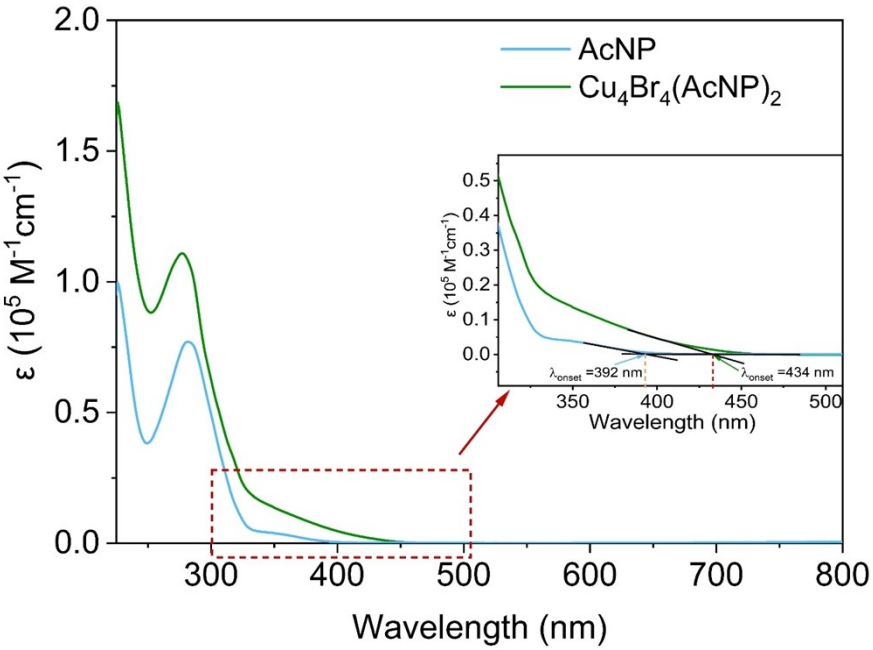

7 Photophysical Properties

Fig. S3 Absorption and PL spectra measured in dichloromethane (c = 2 × 10^{-5} M) at room temperature. Inset indicates onset wavelengths (λ_{onset}) of the absorption spectra. The intersections of dot tangent lines indicate the onset wavelengths.

Fig. S4 Emission spectra of $Cu_4Br_4(AcNP)_2$ in 40 wt%-doped BCPO films (left) and $Cu_4Br_4(AcNP)_2$ neat films (right) from 77 K to 300 K.

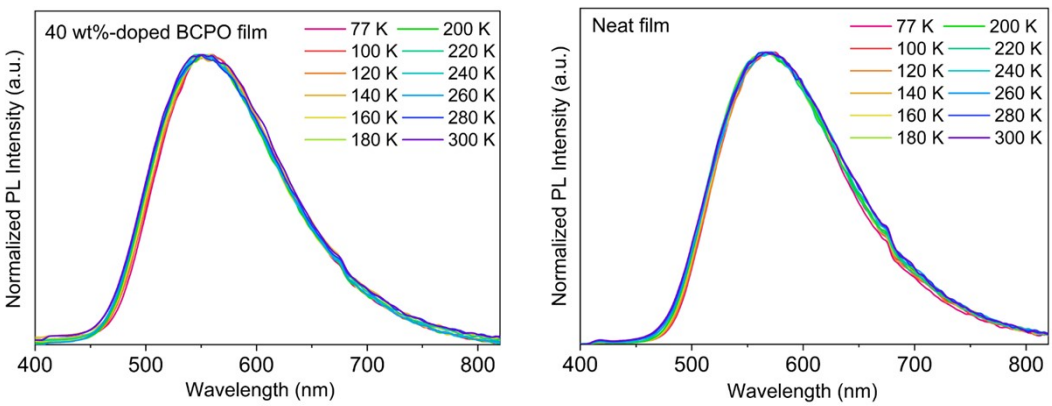

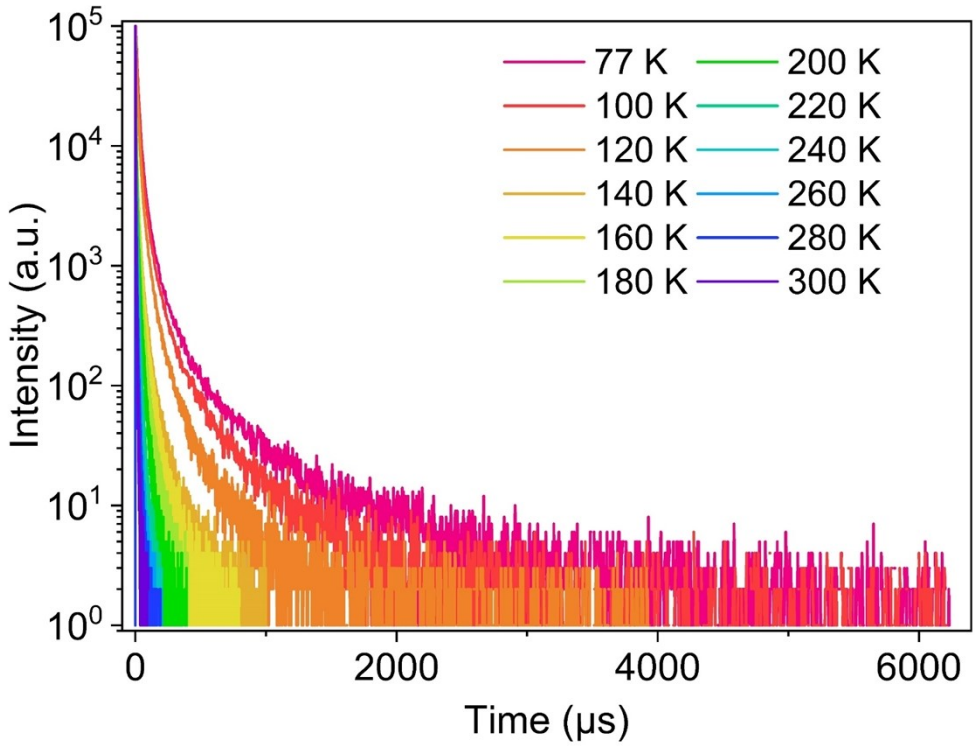

Fig. S5 Photoluminescence decay curves of $Cu_4Br_4(AcNP)_2$ neat film at different

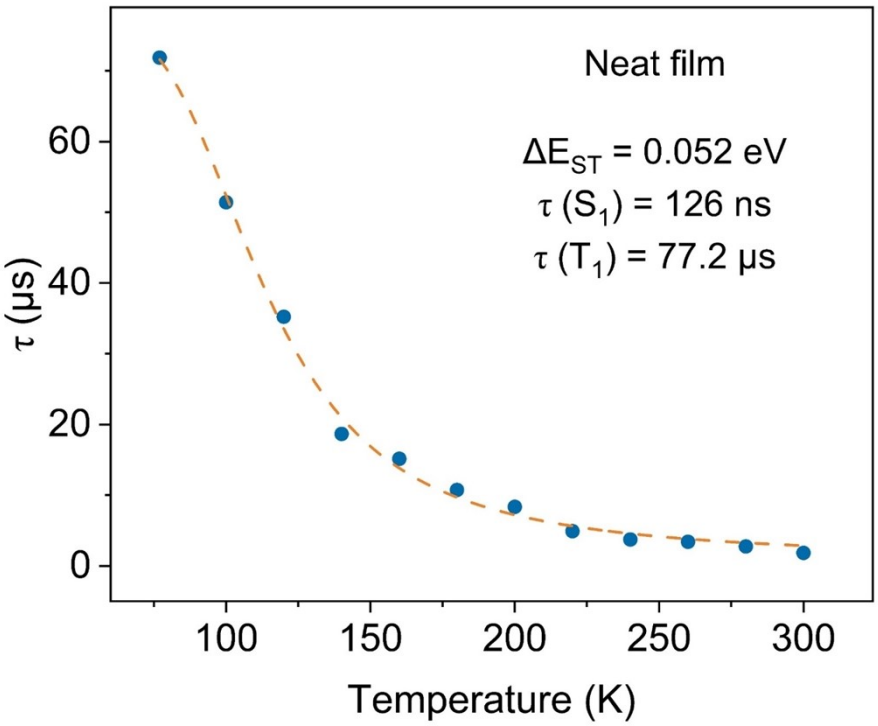

temperatures.

Fig. S6 Temperature dependence of the decay time of $Cu_4Br_4(AcNP)_2$ neat films.

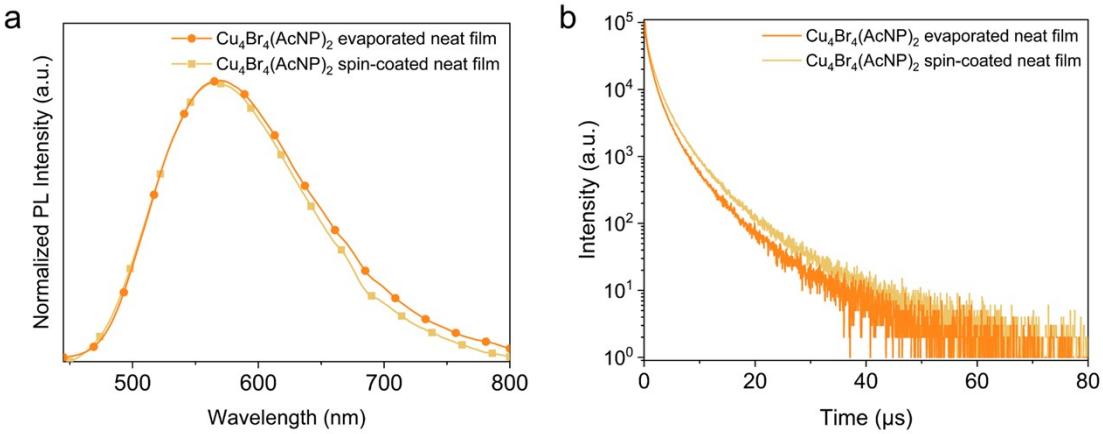

Fig. S7 Emission spectra (a) and Photoluminescence decay curves (b) of $Cu_4Br_4(AcNP)_2$ evaporated neat film and $Cu_4Br_4(AcNP)_2$ spin-coated neat film at room temperature.

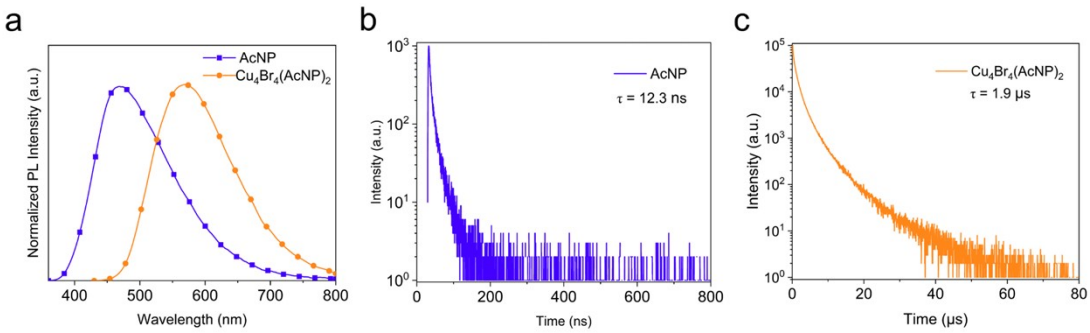

Fig. S8 a) Emission spectra of AcNP neat film and $Cu_4Br_4(AcNP)_2$ neat film at room temperature; b) Photoluminescence decay curve of AcNP neat film at room temperature; c) Photoluminescence decay curve of $Cu_4Br_4(AcNP)_2$ neat film at room temperature.

8 Device Fabrication and Characterization

Indium tin oxide (ITO) glass was ultrasonic cleaned with detergent, deionized water, acetone and ethanol for 15 minutes, washed with dry nitrogen to remove the solvent on the surface, and finally treated with ultraviolet ozone for 15 minutes. Subsequently, TAPC, mCP, DPEPO, TmPyPB and EML were successively deposited on the multilayer device by vacuum thermal evaporation in an inert chamber less than 1×10^{-5} Pa. In another inert chamber with a pressure of less than 2×10^{-4} Pa, Liq and Al are deposited on a multilayer device by vacuum thermal evaporation. The intersection of ITO and Al electrodes gave an active device area of 9 mm^2. EL spectra, CIE coordinates, CE, PE, EQEs and current density-voltage-luminance curves (I-V-L) of OLEDs were measured by an integrated photoelectric performance test system consisting of a calibrated spectral radiometer (TOPCON SR-UL1R) and a Keithley 2400 light source meter.

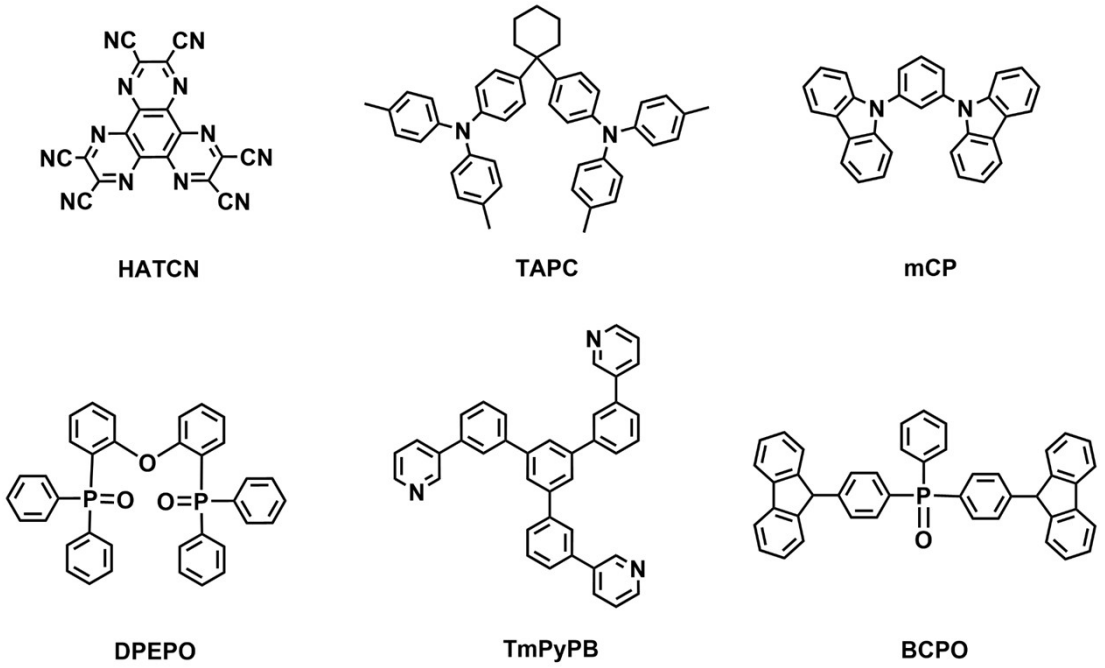

Fig. S9 Molecular structures of the functional materials used in the OLEDs.

Table S7 Summary of the performance of state-of-the-art non-doped OLEDs utilizing Cu(I) emitters.

Emitter	ref.	λ_{EL}[a] nm	L_{max}[b] cd/m^2	EQE[c] %	CE[d] cd/A	PE[e] lm/W
$[Cu(\mu\text{-}I)dppb]_2$	5	544	8019	8.3	25.2	22.9
$[CuBr(dpts)(PPh_3)]$	6	564	234	7.7	/	/
CTC	7	606	1200	4.0	7.21	7.55
$[DDMACDBFDP]_2Cu_4I_4$	8	508	/	9.5	/	/
$[TMeOPP]_4Cu_4I_4$	9	533	87.5	2.6	8.7	8.6
CuMAC Cz	10	555	41000	16.3	/	/
This work		572	1045	10.2	27.0	25.3

[a] EL emission peak wavelength; [b] maximum luminance; [c] EQE maximum value; [d] maximum current efficiency (CE); [e] maximum power efficiency (PE).

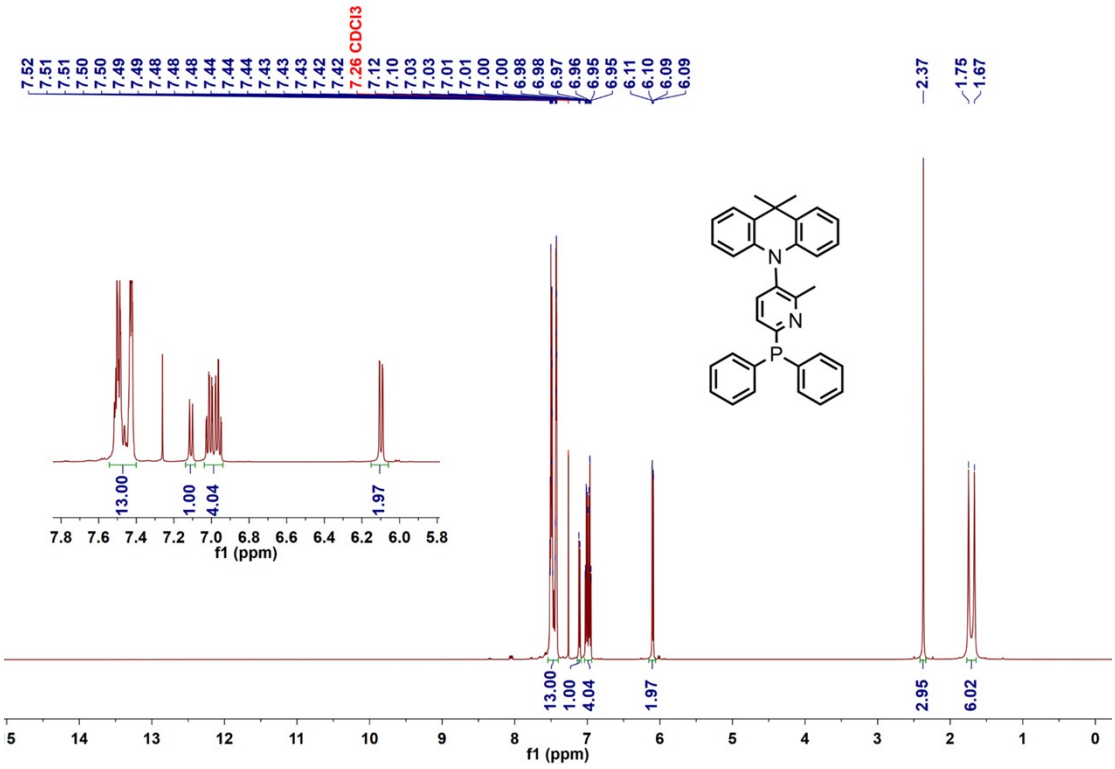

9 NMR Spectra

Fig. S10 ^{1}H-NMR spectrum of AcNP in $CDCl_3$.

Fig. S11 ^{1}H-NMR spectrum of $Cu_4Br_4(AcNP)_2$ in DMSO-d_6.

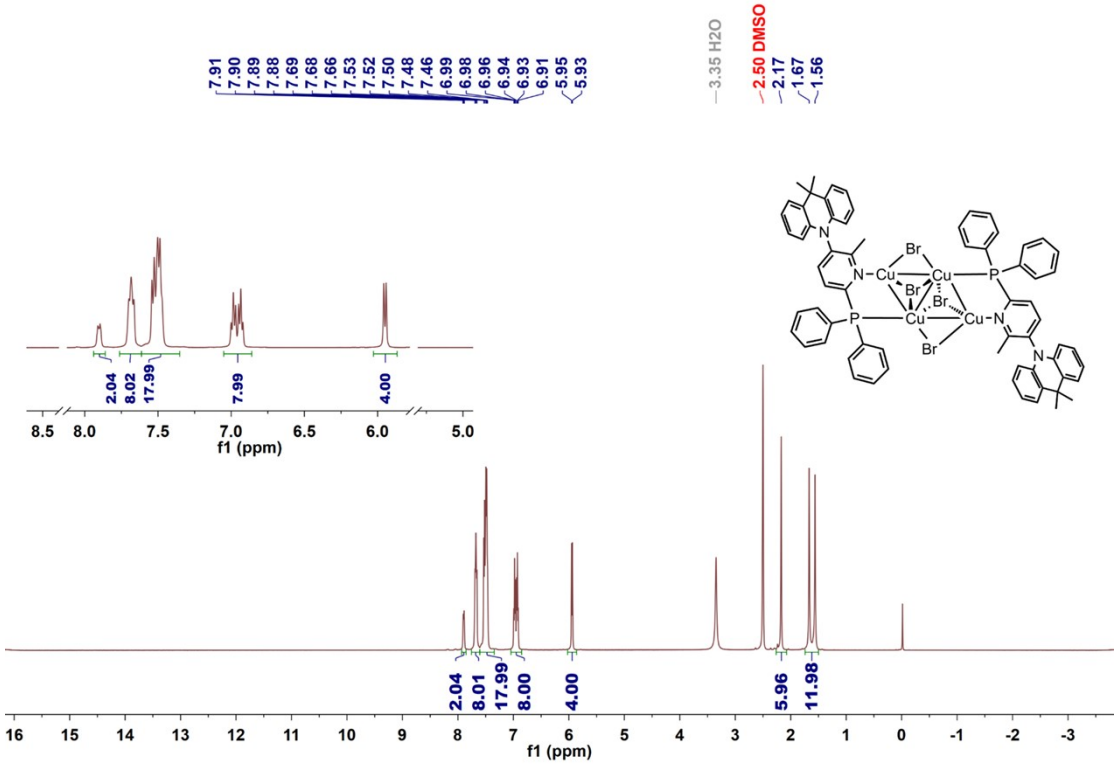

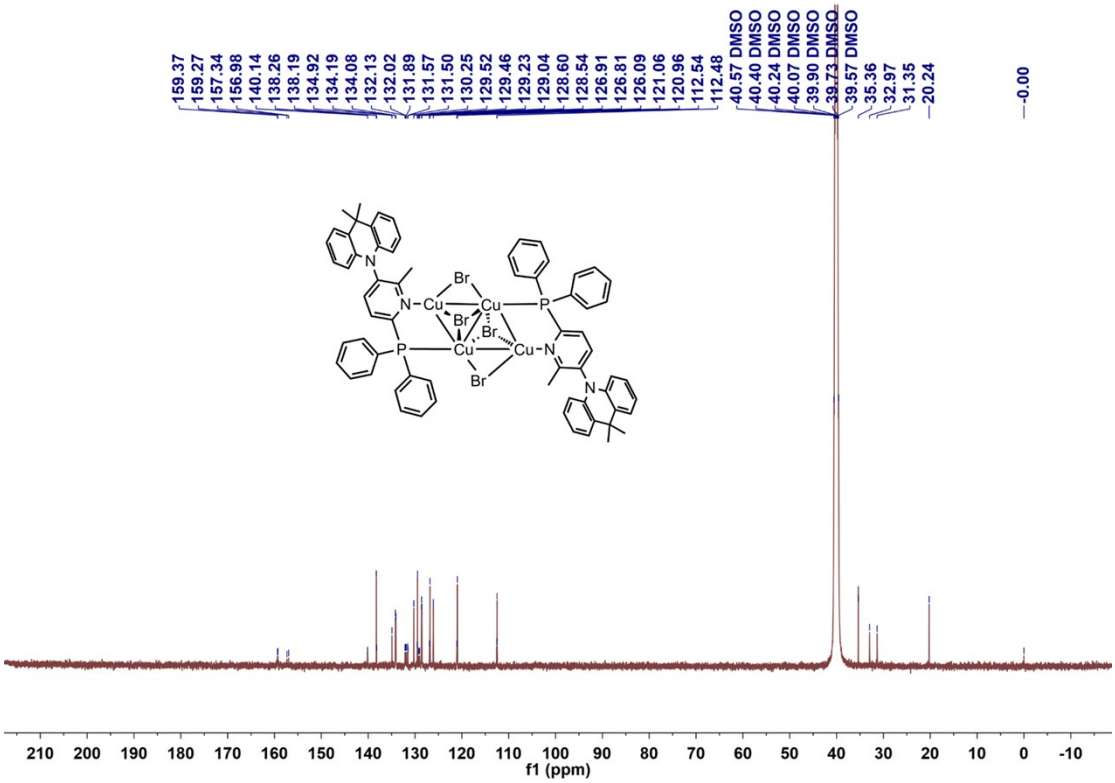

Fig. S12 ^{13}C-NMR spectrum of $Cu_4Br_4(AcNP)_2$ in DMSO-d_6.

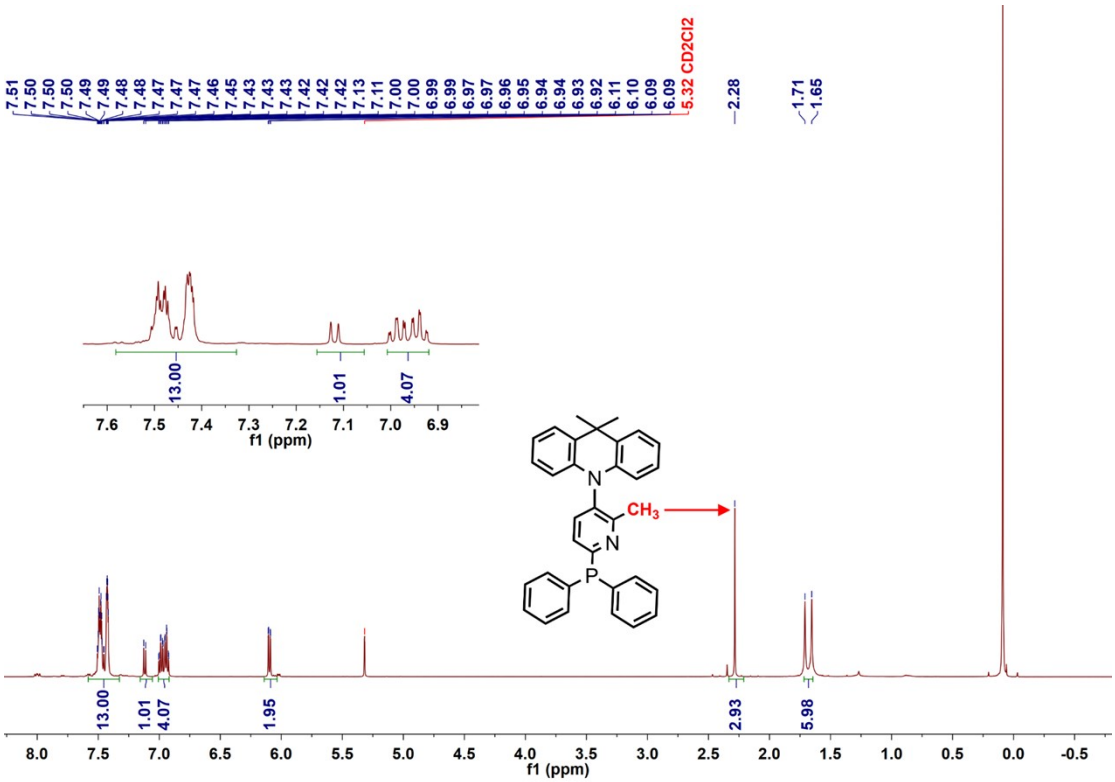

Fig. S13 ^{1}H-NMR spectrum of AcNP in CD_2Cl_2.

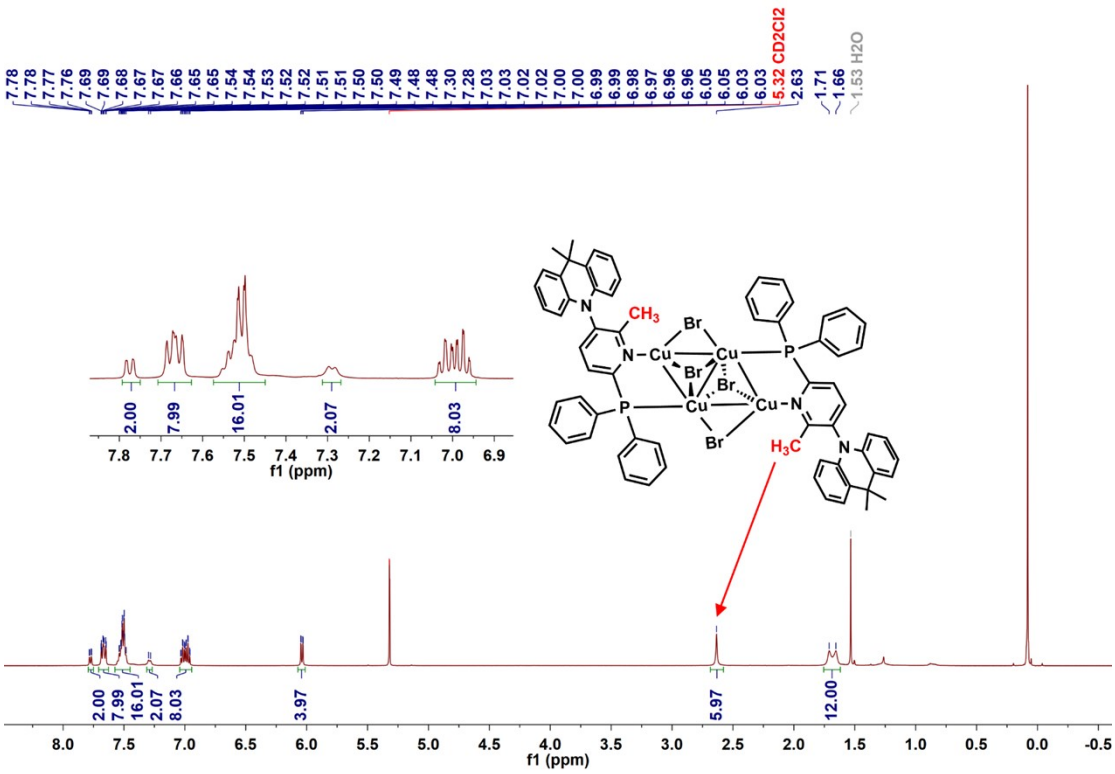

Fig. S14 ^{1}H-NMR spectrum of $Cu_4Br_4(AcNP)_2$ in CD_2Cl_2 before evaporation.

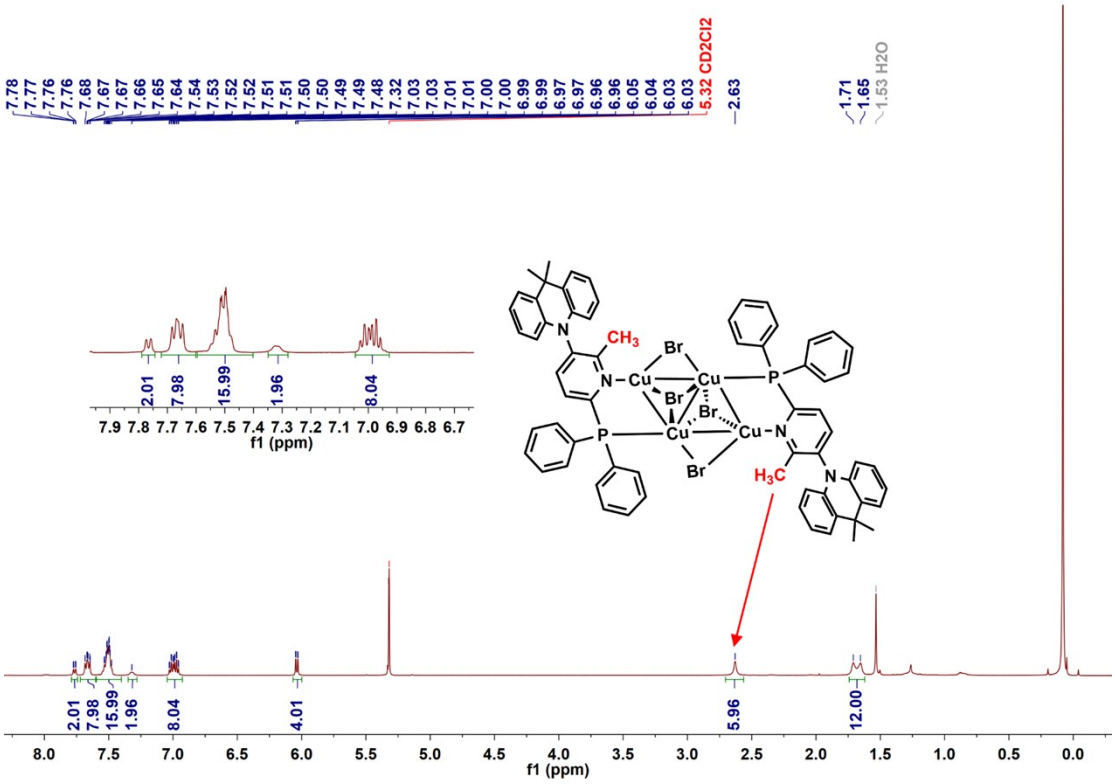

Fig. S15 ^{1}H-NMR spectrum of $Cu_4Br_4(AcNP)_2$ in CD_2Cl_2 after evaporation.

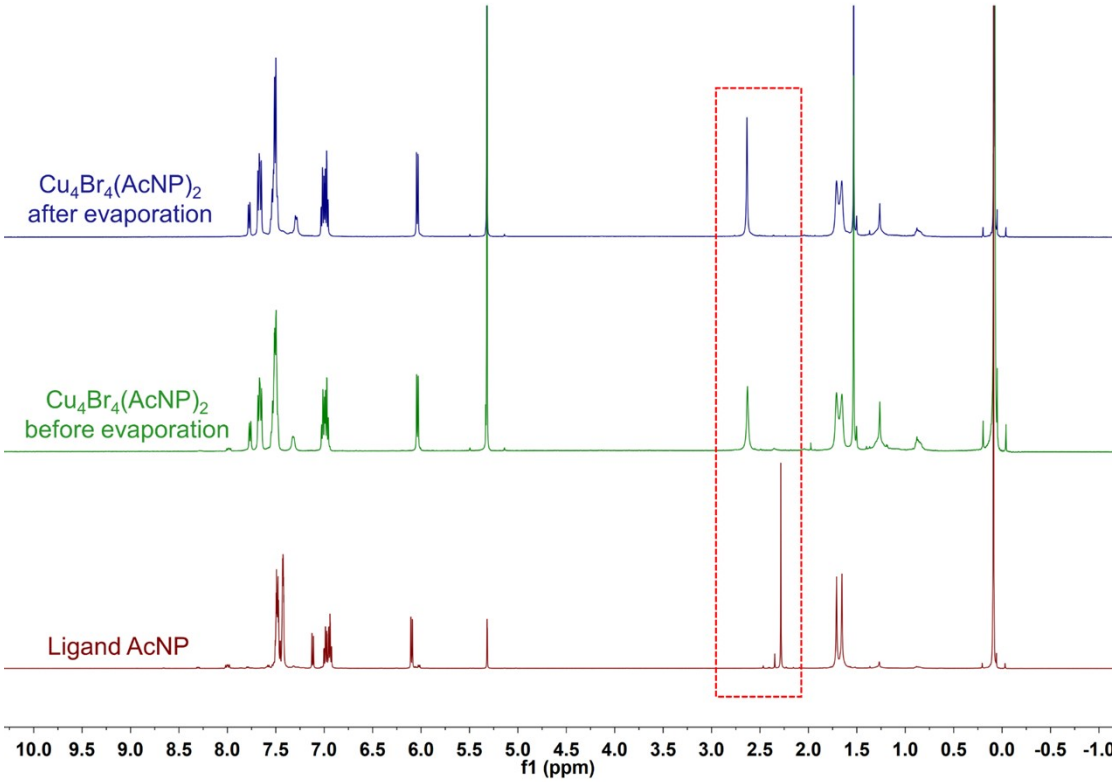

Fig. S16 Stack diagram comparing the ^{1}H-NMR spectra of the ligand AcNP in CD_2Cl_2 with the ^{1}H-NMR spectra of $Cu_4Br_4(AcNP)_2$ in CD_2Cl_2 before and after evaporation (dashed lines indicate the chemical shift of hydrogen atoms on the methyl groups within the pyridine ring of AcNP).

10 Reference

1 J.-H. Jia, D. Liang, R. Yu, X.-L. Chen, L. Meng, J.-F. Chang, J.-Z. Liao, M. Yang, X.-N. Li and C.-Z. Lu, Coordination-Induced Thermally Activated Delayed Fluorescence: From Non-TADF Donor–Acceptor-Type Ligand to TADF-Active Ag-Based Complexes, *Chem. Mater.*, 2020, **32**, 620-629.

2 L. J. Kang, J. Chen, T. Teng, X. L. Chen, R. M. Yu and C. Z. Lu, Experimental and theoretical studies of highly emissive dinuclear Cu(I) halide complexes with delayed fluorescence, *Dalton T*, 2015, **44**, 11649-11659.

3 G. W. T. M. J. Frisch, H. B. Schlegel, G. E. Scuseria, M. A. Robb, J. R. Cheeseman, G. Scalmani, V. Barone, B. Mennucci, G. A. Petersson, H. Nakatsuji, M. Caricato, X. Li, H. P. Hratchian, A. F. Izmaylov, J. Bloino, G. Zheng, J. L. Sonnenberg, M. Hada, M. Ehara,

K. Toyota, R. Fukuda, J. Hasegawa, M. Ishida, T. Nakajima, Y. Honda, O. Kitao, H. Nakai, T. Vreven, J. A. Montgomery Jr., J. E. Peralta, F. Ogliaro, M. Bearpark, J. J. Heyd, E. Brothers, K. N. Kudin, V. N. Staroverov, R. Kobayashi, J. Normand, K. Raghavachari, A. Rendell, J. C. Burant, S. S. Iyengar, J. Tomasi, M. Cossi, N. Rega, J. M. Millam, M. Klene, J. E. Knox, J. B. Cross, V. Bakken, C. Adamo, J. Jaramillo, R. Gomperts, R. E. Stratmann, O. Yazyev, A. J. Austin, R. Cammi, C. Pomelli, J. W. Ochterski, R. L. Martin, K. Morokuma, V. G. Zakrzewski, G. A. Voth, P. Salvador, J. J. Dannenberg, S. Dapprich, A. D. Daniels, Ö. Farkas, J. B. Foresman, J. V. Ortiz, J. Cioslowski and D. J. Fox, Gaussian 09, Revision D.01, Gaussian, Inc., Wallingford, CT, 2009.

4 T. Lu and F. Chen, Multiwfn: A multifunctional wavefunction analyzer, *J Comput Chem*, 2011, **33**, 580-592.

5 F. Wei, T. Zhang, X. Liu, X. Li, N. Jiang, Z. Liu, Z. Bian, Y. Zhao, Z. Lu and C. Huang, Efficient nondoped organic light-emitting diodes with Cu I complex emitter, *Org. Electron*, 2014, **15**, 3292-3297.

6 B.-K. Guo, F. Yang, Y.-Q. Wang, Q. Wei, L. Liu, X.-X. Zhong, L. Wang, J.-K. Gong, F.-B. Li, W.-Y. Wong, K. A. Alamry and Y. Zhao, Efficient TADF-OLEDs with ultra-soluble Copper(I) halide complexes containing non-symmetrically substituted bidentate phosphine and PPh_3 ligands, *J. Lumin*, 2020, **220**, 116963.

7 H. Yang, J. Zheng, M. Xie, D. Luo, W.-J. Tang, S.-K. Peng, G. Cheng, X. Zhang, X.-P. Zhou, C.-M. Che and D. Li, Aggregation-Enhanced Emission in a Red Cu(I) Emitter with Quantum Yield >99%, *ACS Materials Letters*, 2022, **4**, 1921-1928.

8 N. Zhang, Y. Li, S. Han, Y. Wei, H. Hu, R. Huo, C. Duan, J. Zhang, C. Han, G. Xie and H. Xu, Cluster Light‐Emitting Diodes Containing Copper Iodine Cube with 100 % Exciton Utilization Using Host‐Cluster Synergy, *Angew.Chem. Int. Ed.*, 2023, **62**, e202305018..

9 Y. Li, S. Xu, X. Zhang, Y. Man, J. Zhang, G. Zhang, S. Chen, C. Duan, C. Han and H. Xu, Bulk Passivation Enables Hundredfold‐Enhanced Electroluminescence of Monophosphine Cu_4I_4 Cubes, *Angew.Chem. Int. Ed.*, 2023, **62**, e202308410.

10 S. Shi, M. C. Jung, C. Coburn, A. Tadle, D. Sylvinson M. R, P. I. Djurovich, S. R.

Forrest and M. E. Thompson, Highly Efficient Photo- and Electroluminescence from Two-Coordinate Cu(I) Complexes Featuring Nonconventional N-Heterocyclic Carbenes, *J. Am. Chem. Soc.*, 2019, **141**, 3576-3588.